Monatsh Chem (2009) 140:985–999
DOI 10.1007/s00706-009-0153-3

REVIEW

Materials design for perovskite SOFC cathodes

Jörg Richter · Peter Holtappels · Thomas Graule · Tetsuro Nakamura · Ludwig J. Gauckler

Received: 23 December 2008 / Accepted: 24 March 2009 / Published online: 16 May 2009
© Springer-Verlag 2009

Abstract This article focuses on perovskite materials for application as cathode material in solid oxide fuel cells. In order to develop new promising materials it is helpful to classify already known perovskite materials according to their properties and to identify certain tendencies. Thereby, composition-dependent structural data and materials properties are considered. Structural data under consideration are the Goldschmidt tolerance factor, which describes the stability of perovskites with respect to other structures, and the critical radius and lattice free volume, which are used as geometrical measures of ionic conductivity. These calculations are based on the ionic radii of the constituent ions and their applicability is discussed. A potential map of perovskites as a tool to classify simple ABO_3 perovskite materials according to their electrical conduction behavior is critically reviewed as a structured approach to the search for new cathode materials based on more complex perovskites with A and/or B-site substitutions. This article also covers the approaches used to influence electronic and the ionic conductivity. The advantage of mixed ionic electronic conductors in terms of the oxygen exchange reaction is addressed and their important properties, namely the oxygen-exchange coefficient and the oxygen diffusion coefficient, and their effect on the oxygen reduction reaction are presented.

Keywords Electrochemistry · Oxides · Membranes · Fuel cells · Structural field map

J. Richter · P. Holtappels (✉) · T. Graule
Laboratory for High Performance Ceramics, Empa, Swiss Federal Laboratories for Materials Testing and Research, Ueberlandstrasse 129, 8600 Duebendorf, Switzerland
e-mail: peter.holtappels@empa.ch

T. Nakamura
Department of Applied Chemistry, Faculty of Engineering, Kanagawa Institute of Technology, Atsugi, Japan

L. J. Gauckler
Department of Materials, ETH Zurich, Wolfgang Pauli-Strasse 10, 8093 Zurich, Switzerland

Introduction

General considerations

Fuel cells are energy-conversion devices, which produce electricity and heat by electrochemically combining fuel and oxidant [1] without the Carnot limitation. High-temperature fuel cells, for example solid oxide fuel cells (SOFC), operate between 600 °C and 1,000 °C and can utilize hydrogen, natural gas, or hydrocarbons.

Figure 1 shows the principle of an SOFC. The porous electrodes (anode: fuel, cathode: oxidant) are separated by a gastight electrolyte. With the aid of electrons the oxygen in the oxidant (e.g. air, O_2) will be reduced to oxygen ions O^{2-} at the cathode side (Eq. 1). The oxygen ions will be incorporated into the electrolyte material which is an oxygen ion conductor and therefore permits only the oxygen ions to pass through towards the anode side. There the oxygen ions combine with the fuel (e.g. H_2, CH_4, CO) in a so-called cold combustion process to form water and, if carbon-containing fuels are involved, CO_2. During this oxidation reaction (Eq. 2) electrons are released and lead via an external circuit to the cathode side where reduction of the oxygen proceeds. Thus, electrical power can be obtained from the cell. The force driving the overall cell reaction is the difference between the chemical potentials of oxygen at the cathode and anode sides. This can be expressed as a difference between the oxygen partial

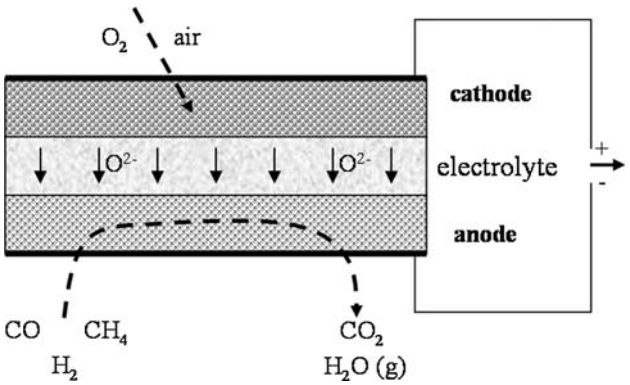

Fig. 1 Principle of the solid oxide fuel cell

pressures and is described by the Nernst equation (Eq. 3), with E_r being the reversible cell voltage, R the gas constant, T the temperature, F the Faraday constant, $p(O_2)$ the partial pressure of oxygen, and where the indices c and a refer to the states at the cathode and the anode, respectively.

$$O_2 + 4e^- \leftrightarrow 2O^{2-} \quad (1)$$

$$2H_2 + 2O^{2-} \leftrightarrow 2H_2O + 4e^- \quad (2)$$

$$E_r = \frac{RT}{4F} \ln \frac{p(O_{2c})}{p(O_{2a})} \quad (3)$$

SOFCs are sometimes referred to as ceramic fuel cells, because they mainly consist of ceramics which can handle high temperatures (>1,000 °C) and therefore facilitate rapid electrode kinetics resulting in the use of nonprecious materials [2] instead of electrodes based on noble metals used in former times [3]. Further, it is possible to use hydrocarbons as fuel (with the aid of internal reforming). The heat produced while operating the SOFC can be used in a variety of cogeneration applications [4]. However, high operation temperatures cause degradation phenomena because of unfavorable reactions of adjacent cell components and sealing difficulties which shorten the lifetime of SOFC systems. Therefore, research nowadays aims at the development of intermediate-temperature SOFCs (IT-SOFC, 600–800 °C) and low-temperature SOFCs (LT-SOFC, $T < 600$ °C) to overcome these problems caused by high temperatures. Therefore, lowering the operating temperature can improve long-term stability and production processes; on the other hand it increases electrochemical losses, because the electrode kinetics and transport processes are mostly thermally activated. This is especially true for oxygen reduction at the SOFC cathode.

Cathode materials should possess high electrical conductivity and high electrocatalytic activity for the oxygen reduction reaction [5]. Further, the compatibility with adjacent cell components and the chemical and dimensional stability during cell operation are very important factors. Moreover, the cathode material should also be sufficiently porous to facilitate transport of the oxidant to the cathode/electrolyte interface [6]. In addition, the perovskites should be stable at the intermediate and lower temperatures used for operation of fuel cells and in CO_2-containing atmospheres [7]. For many years the perovskite $La_{1-x}Sr_xMnO_{3-\delta}$ (LSM) has been the state-of-the-art material because it satisfactorily fulfills the aforementioned cathode-requirements. However, aiming towards IT-SOFCs and/or LT-SOFCs introduces severe performance problems. The main factor limiting the performance in an IT-SOFC is the oxygen reduction reaction at the cathode [8, 9]. A better understanding of the processes at the cathode is needed to apply strategies for optimizing the materials [10]. One step to overcome polarization resistances has been the introduction of composite electrodes (a mixture of a solid electrolyte and an electronic conductor) or a material offering both ionic and electronic conduction (mixed ionic electronic conductor, MIEC) [11]. Use of this approach was thought to increase the active area for reduction of oxygen, because for pure electronic conductors this reaction was limited to the three-phase boundary (TPB), where electrolyte, electrode, and gaseous phase meet. There the reduction of the oxygen molecules takes place and the oxygen ions enter the electrolyte material. Hence substantial ionic conductivity of the MIEC material opens the pathway for oxygen ion migration also through the MIEC itself [12] and therefore spreads the possible reaction zone.

During recent decades there has been substantial interest in identifying the best material for application as the cathode material in a solid oxide fuel cell. Materials like $La_{1-x}Sr_xMnO_{3-\delta}$ (LSM), $La_{1-x}Sr_xFeO_{3-\delta}$ (LSF) or $La_{1-x}Sr_xCoO_{3-\delta}$ (LSC) and mixtures thereof, for example $La_{1-x}Sr_xCo_{1-y}Fe_yO_{3-\delta}$ (LSCF) have been investigated in detail. LSM used to be the material of choice because it provides excellent electronic conductivity (200–300 S/cm at 900 °C) [13]. However, the ionic conductivity is very low (10^{-7} S/cm at 900 °C) [13, 14]. Because of the poor electrocatalytic activity of LSM, its application in IT-SOFCs is seriously limited. Research nowadays aims at developing cathode materials with higher electrocatalytic activity than LSM [15]. To compete with the performance of MIECs as cathode materials, LSM is preferably used in composite cathodes, where the ionic conductivity is supplied by an oxygen ion conductor as in Ni-YSZ-cermets. By contrast, LSF provides electronic and ionic conduction and therefore seems to be a promising candidate as IT-SOFC cathode material [16] by increasing the TPB-area. The maximum conductivity of $La_{1-x}Sr_xFeO_{3-\delta}$ occurs at approximately $x = 0.5$ and reaches more than 350 S/cm at 550 °C. With increasing temperatures the conductivity

decreases [17]. Nevertheless, LSF electrodes exhibit promising electrocatalytic properties, because incorporation of iron enhances oxygen diffusion and surface exchange processes [10]. LSC shows extraordinary electronic conduction up to 1,600 S/cm at 800 °C [18], but it seems to be unsuitable for high-temperature applications, because its coefficient of thermal expansion (CTE) does not match the impressive values achieved for state-of-the-art electrolytes, for example yttria-stabilized zirconia (YSZ) [19]. At lower temperatures the conductivity of $LaCoO_{3-\delta}$ has a positive temperature coefficient but it seems to be metallic at elevated temperatures [18]. On increasing x in $La_{1-x}Sr_xCoO_{3-\delta}$ the transition to metallic behavior occurs at lower temperatures [18, 20]. An increasing amount of strontium also leads to an increase of the CTE [18]. On the one hand, incorporation of iron into LSC reduces the CTE but, on the other hand, also reduces the conductivity [18]. LSCF has a total conductivity of 230 S/cm at 900 °C, similar to LSM [21], but also has oxygen ionic conductivity of approximately 0.2 S/cm [22]. On the one hand, substitution of Fe ions for Co ions in LSC reduces available hopping sites which seriously limits electronic conduction. However, on the other hand, Fe ions are more stable against oxidation when divalent cation substitution occurs at the A site. Therefore, the concentration of oxygen vacancies is increased and oxygen diffusion via vacancies is facilitated [10]. Because of its very good oxygen surface exchange and diffusion properties BSCF has been applied as material for oxygen separation membranes until it was also suggested as an SOFC cathode material [23, 24]. However, the conductivity of $Ba_{0.5}Sr_{0.5}Co_{0.6}Fe_{0.4}O_{3-\delta}$ does not exceed 23 S/cm at 800 °C in air [25]. Under the same conditions the total conductivity of $PrMnO_{3-\delta}$ reaches 80 S/cm and can be increased to 250 S/cm for $Pr_{0.5}Sr_{0.5}MnO_{3-\delta}$ [26]. However, the aforementioned materials still suffer from different problems and research in alternative materials with superior properties at intermediate temperatures is still ongoing [1, 23].

Affecting the perovskite properties

Because it is well known that the perovskite structure can tolerate extensive modifications with regard to composition, researchers partly substitute the A and/or the B-site cations of the perovskite ABO_3 to enhance specific properties such as conductivity, catalytic activity, compatibility, and/or stability. This leads to numerous substances which are considered to be potential SOFC cathode materials. However, published data often show a lack of agreement [27, 28]. Here we try to give an overview of basic principles for choosing an appropriate perovskite material for a specific application. Thereby, the article covers approaches used to predict the existence of the perovskite structure ABO_3 as a function of composition, and strategies used to affect the type and magnitude of their electrical conductance. Emphasis is placed on structural approaches to classification of perovskite materials.

Structural field maps for perovskites

The perovskite structure has the general formula ABX_3. The ideal perovskite structure is cubic with the larger A-site cations located at the corners of the cube, the B-site ions at the body center, and the oxygen ions at the centers of the faces. As shown in Fig. 2 the A-site ion of a perovskite structure is coordinated by twelve oxygen ions whereas the ion located at the B site has sixfold coordination. Perovskite structures can withstand wide variations of the elements at the A and B sites.

The stability of perovskites relative to other structures is frequently defined in terms of the Goldschmidt tolerance factor t (Eq. 4, r_A, r_B, and r_O are the radii of the A-site cation, the B-site cation, and the oxygen ion, respectively). Stable perovskite structures are predicted for $0.77 \leq t \leq 1.00$ [29]. Designing t close to unity leads to higher symmetry and smaller unit cell volumes [30]. The perfect cubic structure ($t = 1$) is achieved when the A-site cation has the same size as the oxygen ion (1.40 Å). These form cubic closest packing and the B-site cations are located in the octahedral holes formed only by oxygen [31]. In a perfect cubic perovskite structure the B–O–B chains are linear, i.e. the bond angle is 180°. Deviation from cubic symmetry results in tilting of the BO_6 octahedra and, therefore, in reduced B–O–B bond angles. For $t > 1$ the hexagonal structures tend to be stable [29] whereas for $t < 1$ the lattice structure changes from cubic to rhombohedral and then to orthorhombic [32].

$$t = \frac{r_A + r_O}{\sqrt{2}(r_B + r_O)} \tag{4}$$

Other approaches used to classify perovskite structures also rely on the radii of the constituent ions, like the Goldschmidt tolerance factor. In an early work Roth [33] classified $A^{2+}B^{4+}O_3$ perovskites on the basis of ionic radii into orthorhombic, pseudocubic, and cubic structures. For the $A^{3+}B^{3+}O_3$ perovskites only rhombohedral and orthorhombic symmetries have been found. Muller and Roy [29] plotted, amongst others, the perovskite structures in structural field maps (diagrams with r_B as abscissa and r_A as ordinate). They also stated that the ideal cubic structure does not occur for the $A^{3+}B^{3+}O_3$ perovskites at room temperature but it does occur for the $A^{2+}B^{4+}O_3$ and the $A^{1+}B^{5+}O_3$ perovskites. Li et al. [34] reviewed the stability ranges of perovskites by using empirical structure

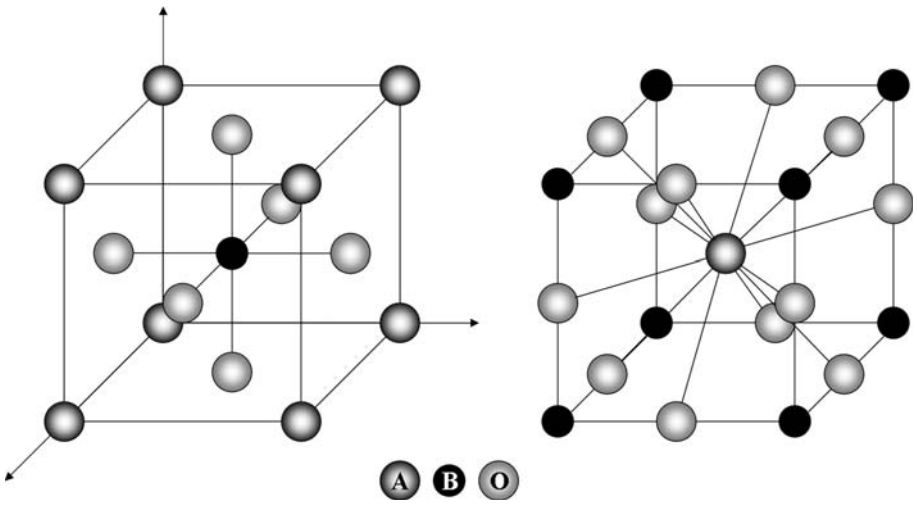

Fig. 2 Structure of an ideal perovskite $A^{2+}B^{4+}X_3$ with $X = O^{2-}$ (*left hand side* A^{2+} in origin; *right hand side* B^{4+} in origin)

map methods and found the octahedral factor, r_B/r_O, to be as important as the tolerance factor t. They constructed a two-dimensional structure map orthogonalizing these two properties and found distinct regions of existence limits of the perovskite structure. Structural field maps serve as helpful tools for predicting the ranges of existence of the perovskite when new elemental combinations are sought. However, technical applications often benefit from optimized properties resulting from subtile replacements of the A as well as the B cations by different cations at the same time resulting in much more complex compositions, for example $A'_{1-x}A''_xB'_{1-y}B''_yO_{3-\delta}$ compared with the simple ABO_3 compounds. None of the aforementioned approaches deals with these substituted perovskites. It is well known that the perovskite structure can accommodate cation substitutions in a wide range, and these usually serve as a targeted modification for tailoring specific properties. This tunability of the perovskite structure offers extensive possibilities for further improvements of the properties of the materials [14], for example electronic and ionic conductivity. Many properties of the perovskites result from the B cations, but are tuned by the A-site cations. The radius of the A-site cation and, especially, its variance were found to be important factors controlling perovskite properties [35]. In order to maintain the perovskite phase when forming solid solutions, the substituting elements should not exceed the structural properties empirically defining the perovskite stability phase fields in the structural field maps.

In order to outline a solid solution phase area accommodating different elements in a structural field map, knowledge of the ionic radii of the elements is important. Several sets of radii have been published (e.g. by Goldschmidt [36], Zachariasen [37], Pauling [38], Ahrens [39], Shannon [40–42]) and differ from each other sometimes by more than 10% [29]. Furthermore, the radius of an ion is strongly dependent on its coordination number and, therefore, upon its near neighborhood structure. In this study, Shannon's [42] ionic radii referring to the coordination numbers 12 (A site) and 6 (B site) have been used, although it is known that an oxygen deficiency influences the coordination number and, therefore, the ionic radii [43].

Goldschmidt's tolerance factor t (Eq. 4) has been calculated with the aid of Shannon's [42] set of ionic radii (Table 1) for model series of perovskites which are known to be promising cathode materials (LSM, LSF, LSC, $La_{1-x}Sr_xCo_{0.5}Fe_{0.5}O_{3-\delta}$, $Ba_{1-x}Sr_xCo_{0.5}Fe_{0.5}O_{3-\delta}$). For more complicated perovskites the radii have been calculated as weighted averages, as already described by Trofimenko et al. [44]. Figure 3 shows the tolerance factor t as a function of the degree of substitution. Addition of Sr^{2+} ions to the A sites increases the tolerance factor if the smaller La^{3+} is substituted but reduces the tolerance factor when the larger Ba^{2+} is replaced. Because of the large A-site cations, the tolerance factors of $Ba_{1-x}Sr_xCo_{0.5}Fe_{0.5}O_{3-\delta}$ are very high.

However, some compositions included in Fig. 3 are relatively close to unity and their structure is supposed to be close to the ideal cubic one with only small distortions. $La_{1-x}Sr_xMnO_{3-\delta}$ follows the trend given in Fig. 3 (increasing structural order with increasing x) and changes from the orthorhombic structure (for $x \leq 0.14$) to the rhombohedral one (for $x \geq 0.18$) [45]. The structure of $La_{0.5}Sr_{0.5}MnO_{3-\delta}$ is reported to be tetragonal [46]. However, the calculated tolerance factor exceeds the value of $t = 1$ for $x \geq 0.55$ and is furthest away from unity for $SrMnO_{3-\delta}$ which shows the hexagonal structure in air and ambient temperature [47].

Under the same conditions the asymmetry of the structure of $La_{1-x}Sr_xFeO_{3-\delta}$ also changes with the amount of strontium. With increasing x the symmetry of the structure changes from orthorhombic ($0 \leq x \leq 0.2$) via rhombohedral

Table 1 Structural data used for calculation of the tolerance factor

Ion	La^{3+}	Pr^{3+}	Sr^{2+}	Ba^{2+}	Co^{3+}	Co^{4+}	Fe^{3+}	Fe^{4+}	Mn^{3+}	Mn^{4+}	In^{3+}
r in Å (CN)	1.360 (12)	1.300 (12)	1.440 (12)	1.610 (12)	0.545 (6)	0.530 (6)[a]	0.645 (6)[a]	0.585 (6)	0.645 (6)[a]	0.530 (6)	0.800 (6)

CN, coordination number

[a] High spin

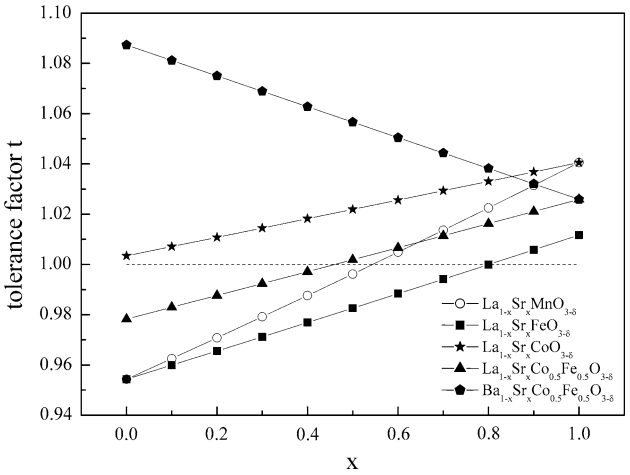

Fig. 3 Evolution of tolerance factor t as a function of A-site substitution with strontium

($0.4 \leq x \leq 0.7$) to cubic ($0.8 \leq x \leq 1.0$) [48]. The trend of the tolerance factors of $La_{1-x}Sr_xCoO_{3-\delta}$ in Fig. 3 is similar to that of LSF but the values are larger and exceed unity, because of the smaller radii of Co^{3+}/Co^{4+} compared with Fe^{3+}/Fe^{4+}. A change of the symmetry from the rhombohedrally distorted ($0 \leq x \leq 0.5$) to the cubic ($0.55 \leq x \leq 0.7$) perovskite phase has been observed [20].

Goldschmidt's tolerance factor is easy to determine and gives a first hint whether the desired composition will form a perovskite structure. Further, it predicts the evolution of a structure depending on the degree of substitution. However, values may exceed the suggested maximum of $t = 1$ for some compositions (e.g. $La_{1-x}Sr_xCoO_{3-\delta}$) although the perovskite phase is still present. Other factors (e.g. temperature, atmosphere) which affect the crystal structure of a material, are not considered in the calculation of the tolerance factor. Nevertheless, with a detailed knowledge of the radii it is possible to design different materials with very similar tolerance factors, i.e. crystal structures. This has been used for instance for designing the oxygen ion conductor $La_{1-x}Sr_xGa_{1-y}Mg_yO_{3-\delta}$ (LSGM). Substitution of Sr^{2+} for La^{3+} increases the tolerance factor whereas substituting Mg^{2+} for Ga^{3+} reduces it again. Therefore, the tolerance factor of LSGM is similar to that of $LaGaO_{3-\delta}$ but the material's properties change drastically because the number of oxygen vacancies is increased [43]. With wise choice of substitution elements the tolerance factor can be designed while properties can be adjusted by, for instance, modifying the defect structure. The reversal conclusion is that it seems difficult to relate other than structural properties (e.g. trends in conductivity) to the tolerance factor [31]. Attfield [35, 49] reported structure–property relationships depending on the A-cation radius. Although the average radius of the A-site cation has been kept constant (and therefore also the tolerance factor is constant), ferroelectric, ferromagnetic, superconducting, and structural transition temperatures show linear dependencies with statistical cation size variance.

Electronic and ionic conductivity

Divalent acceptor substitution for the trivalent A-site cation requires that, because of electroneutrality, the introduced effective negative charge is compensated either by an increase in valence of the B-site cations (electronic compensation) and/or the formation of oxygen vacancies (ionic compensation) [50]. Transition metals (TM) as B-site cations can perform a valence change in order to compensate the introduced charge imbalance and create TM^{4+}/TM^{3+} couples which act as hopping sites for electrons/holes, i.e. for n-type or p-type conductivity. The higher the amount of available hopping sites, the higher the conductivity values expected. Therefore, the theoretical maximum conductivity is expected for 50 mol% divalent acceptor substitution for the trivalent A-site cation. This would result in a maximum TM^{4+}/TM^{3+} ratio of 1:1 if only electronic compensation is assumed [17]. However, the relative proportion between the creation of vacancies and the oxidation of the transition metal ions is temperature [51] and pO_2-dependent and material-specific.

Normally, in perovskites with transition metals on the B site, the electronic conduction is because of their valence change and proceeds along the three-dimensional BO_6 octahedra network, which is stable for substitution of the A site [32]. However, some of the transition metals on the B site behave differently. Manganese-containing perovskites mostly perform electronic compensation whereas it has been shown that incorporation of the transition metal iron into LSM limits the electronic conductivity, because an increasing iron content enhances the ionic compensation. The decrease in the number of Mn^{3+}/Mn^{4+} couples leads to a reduced amount of available hopping sites [10]. In the manganese-free LSF the electrical properties are improved

because of the charge disproportionation Fe^{3+}/Fe^{5+}, as revealed by Mössbauer spectroscopy [10]. A further important defect reaction that occurs is the charge disproportionation reaction by which Mn^{3+} partially disproportionates into Mn^{2+} and Mn^{4+} leading to good electronic conductivity even of stoichiometric $LaMnO_3$ [52]. This reaction can be considered to be entropy-driven and occurs to a significant extent because of the relatively unstable electron configuration of Mn^{3+} [53].

When analyzing the electrical conductance using the Arrhenius plot $\ln(\sigma T)$ versus $1/T$, linear behavior means that the electronic conductivity is because of the small polaron-hopping mechanism which occurs in the perovskite along the transition metal–oxygen–transition metal chains (e.g. Fe^{3+}–O–Fe^{4+}). An activation energy can be extracted by fitting Eq. 5, where σ is the electrical conductivity, C the pre-exponential factor, containing amongst others the charge-carrier concentration, T the absolute temperature, k the Boltzmann constant, and E_a the activation energy representing the enthalpy of polaron migration [54]. The exponent s equals either 1 or 3/2 for adiabatic or non-adiabatic processes, respectively [26].

$$\sigma = (C/T^{s})\exp(-E_a/kT) \tag{5}$$

In order to use the advantages of a mixed ionic electronic conductor the electronic conductivity needs to be supported by a substantial amount of ionic (O^{2-}) conductivity which occurs via the vacancy mechanism. The oxygen ions perform a diffusive jump by exchange of their position with an adjacent vacancy. Vacancies are defects in the oxygen sublattice and there are intrinsic defects which are temperature-dependent and extrinsic defects which are dependent on impurities and/or the level of substitution [55]. As already mentioned, perovskite structures can accommodate cations of a rather wide range of ionic radii and valence. This opens up wide possibilities for aliovalent substitutions. Although the following considerations are mainly meant for electrolyte materials with negligible electronic conductivity, they also serve as a guideline for MIECs. When no multivalent ions are included, any substitution of cations in the perovskite ABO_3 by cations with lower valence states will create oxygen vacancies in order to maintain the charge balance. Increasing amount of oxygen vacancies is expected to increase the oxygen ion conductivity. Substitution of 10% Sr^{2+} for La^{3+} increases the ionic conductivity from 7.3×10^{-5} S/cm for $LaInO_3$ to 1.8×10^{-3} S/cm for $La_{0.9}Sr_{0.1}InO_{2.95}$ [56]. Another example of successful application of this strategy is the SrO and MgO-substituted $LaGaO_3$ which forms $La_{1-x}Sr_xGa_{1-y}Mg_yO_{3-x/2-y/2}$. Without electronic compensation the extent of substitution directly relates to the amount of oxygen vacancies. The composition $La_{0.8}Sr_{0.2}Ga_{0.8}Mg_{0.2}O_{2.8}$ is a very promising oxide ion conductor with an ionic conductivity of 0.14 S/cm at 800 °C (without significant electronic conductivity) [31]. It has been shown that minor amounts of transition metal cations (Co, Fe) in the B sublattice are advantageous in terms of oxygen ionic conductivity [30]. Further addition of transition metal ions leads to increased electronic conductivity, resulting in mixed ionic and electronic conductivity. In MIECs, aliovalent substitution at the A site will also lead to partial oxidation of the transition metal ions located at the B site. However, there are general limits which have to be considered when substituting the constituent ions. Too many vacancies can induce structural deformations or the vacancies can also become ordered, as in brownmillerite structures [51], resulting in a decrease of ionic conductivity.

Ionic conductivity is not only dependent on the presence of vacancies, it is also affected by geometrical factors. Ranløv [57] found better ionic conductivity with higher symmetry, i.e. perovskite structures with tolerance factors close to $t = 1$. While jumping from one site to the adjacent vacancy along the anion octahedra edge [58], the oxygen ion has to pass through a "saddle point" (Fig. 4) which is built by two A-site cations and one B-site cation. Depending on the composition of the perovskite a critical radius r_{cr} can be calculated which describes the maximum size of the mobile ion to pass through. The critical radius can be calculated by using Eq. 6 [59] where r_A and r_B are the radius of the A ion and B ion, respectively, and a_0 corresponds to the pseudo cubic lattice parameter ($V^{1/3}$) which can be derived experimentally or from Eq. 7 [60].

$$r_{cr} = \frac{a_0\left(\frac{3}{4}a_0 - \sqrt{2}r_B\right) + r_B^2 - r_A^2}{2(r_A - r_B) + \sqrt{2}a_0} \tag{6}$$

$$a_0 \approx V_{cell}^{1/3} = 2.37r_B + 2.47 - 2.00(t^{-1} - 1) \tag{7}$$

For typical perovskite materials this critical radius does not exceed 1.05 Å [31]. However, because the radius of the oxygen ion is 1.4 Å in the sixfold coordination there must be significant outward relaxation of the cations (away from

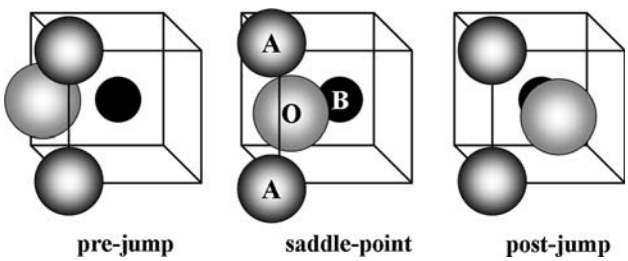

Fig. 4 Saddle point after [61]: two A-site cations and one B-site cation build a gap which is described by the critical radius; the cations show significant outward relaxation to permit the migration of the oxygen ion

the mobile oxygen ion) which reduces repulsive overlap interactions [61]. During the diffusive jump the oxygen ion might temporarily adopt threefold coordination at the position between two A and one B-site cations. Because in threefold coordination the radius of the oxygen ion would still be too large (1.36 Å) to pass through the gap the thermal vibration of the cations is supposed to assist the oxygen ion to migrate. Reducing the mass of the cations increases the amplitude of their thermal vibration and, therefore, enhances the oxygen ionic conductivity [31]. Larger critical radii can be achieved by increasing r_B and/or reducing r_A.

In order to improve the oxygen ion conductivity several other structural properties are discussed in literature. Sammells et al. [62] introduce the lattice free volume, V_f, which is obtained by subtraction of the constituent ion's volumes from the overall crystallographic unit cell volume. Obviously, a larger free volume provides more space for the mobile ions to move more easily and therefore reduces the activation energy for anion migration [63]. To compare various kinds of perovskite oxides the specific free volume (free volume divided by the unit cell volume) was introduced by Hayashi et al. [43]. Large specific free volumes are desirable to obtain larger oxygen ion mobilities. Although the approaches using the lattice free volume and the critical radius give certain tendencies, there are exceptions. Lybye et al. [64] investigated $La_{0.9}Sr_{0.1}B_{0.9}Mg_{0.1}O_{2.9}$ perovskites (B = Al^{3+}, Ga^{3+}, Sc^{3+}, In^{3+}) in terms of their conductivity and tried to relate properties that are thought to influence the ionic conductivity. Those properties include, among others, the tolerance factor, the lattice free volume, and the critical radius. Calculations of the lattice free volume and the critical radius suggest that the indium-containing perovskite should be the best ionic conductor whereas the tolerance factor points towards $La_{0.9}Sr_{0.1}Al_{0.9}Mg_{0.1}O_{2.9}$. Finally, the gallium-containing perovskite had the highest oxygen ionic conductivity, so Mogensen et al. [31] looked for other properties describing the ionic conductivity of perovskites. They concluded that a stress-free lattice is the key factor for fast oxygen ion conductors. Cubic symmetry provides stress-free lattices which induce the oxygen sites to be equivalent [43]. Increasing lattice distortion leads to a high degree of anisotropy of oxygen sites [65] which hampers the jump of oxygen ions. The conductivity decreases with the deviation from the ideal cubic symmetry [51]. Therefore, substitutions of cations should be done in a considerate manner, i.e. the size mismatch between host and substituting cations should be minimized in order to keep the structure as distortion-free as possible. Further factors which are supposed to favor high ionic conductivity are a low mean value of metal–oxygen bonding energy [51] of the overall lattice and minimal polarization of the mobile species by the lattice [62]. The interaction between the oxygen ion and the B-site ion is expected to increase with the valence state of the B-site cation, i.e. the best oxide ion conductivities should be found within the $A^{3+}B^{3+}O_3$ perovskites [31].

Figure 5 shows the evolution of r_{cr} for the same set of perovskites as already shown in Fig. 3. The trends show the opposite behavior when compared with the evolution of the tolerance factor. A larger ionic radius at the A site (e.g. Sr^{2+} substitutes La^{3+}) reduces the critical radius whereas it increased the tolerance factor. As already mentioned, the critical radius should be as large as possible in order to enhance oxygen ionic conductivity. On the one hand, substitution of Sr^{2+} for La^{3+} reduces the critical radius, which suggests a decrease in ionic conductivity, but on the other hand it introduces oxygen vacancies which, as previously mentioned, enhance the ionic conductivity. As described for $La_{1-x}Sr_xCo_{0.8}Fe_{0.2}O_{3-\delta}$ the ionic conductivity increased monotonically with increasing x [22]. This indicates vacancy formation to be more important than the critical radius. Therefore, it is more valuable to compare the critical radius of different compositions with the same amount of oxygen vacancies rather than evolution of the critical radius as a function of A-site substitution.

Although LSCF and, especially, BSCF show low values for the critical radius, both compositions are known to be good oxygen ion conductors compared with other perovskites. The LSF series itself exhibits large critical radii which are rapidly decreased when Co is substituted for Fe. Therefore, the model series $La_{1-x}Sr_xCo_{0.5}Fe_{0.5}O_{3-\delta}$ in Fig. 5 shows average critical radii. Iron-containing perovskites rather perform the ionic compensation, i.e. instead of a valence change of the transition metal oxygen vacancies are created. Therefore, the ionic conductivities might be good although indicated differently by the plot of the critical radius. Despite their large critical radii (especially

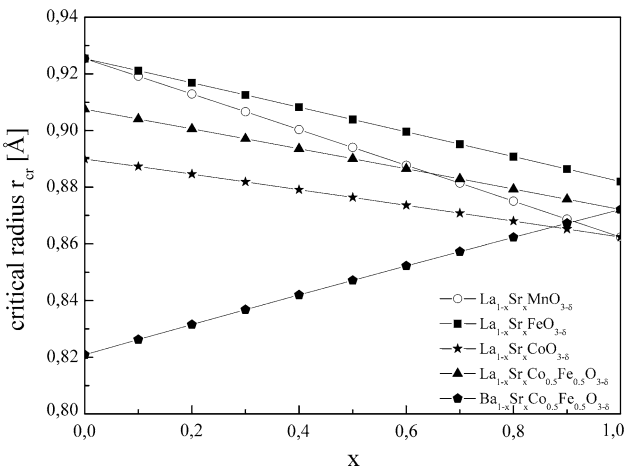

Fig. 5 Evolution of critical radius r_{cr}

for low substitution rates) the LSM materials do not show good ionic conductivities. This is because of the relatively easy valence change of the Mn ion which immediately equilibrates a charge imbalance introduced by a substitution of La^{3+} by Sr^{2+} instead of creating oxygen vacancies which are the prerequisite for the oxygen ion migration. If multivalent ions are included it is complicated to estimate the relationship of electronic to ionic compensation. Without experiments (thermogravimetric analyses) or defect chemistry modeling it is difficult to figure out compositions with a similar amount of oxygen vacancies and to compare them in terms of their critical radius.

The tolerance factor t, critical radius r_{cr}, lattice free volume V_f, and specific free volume already described are calculated from the two variables r_A and r_B. The average metal–oxygen bond energy is, next to the cation charges, also dependent on the ionic radii. Therefore, some redundancy between these properties is expected. It is impossible to vary one without also varying the others [65]. As can be seen from Figs. 3 and 5, the tolerance factor and the critical radius (and, with these, the free volume also) show opposite trends. Finding the optimum material will be a compromise: for instance the specific free volume can only be increased at the expense of a departure from cubic symmetry [43]. Another indicator for the need to balancing different properties is the following: as described, the optimum material in terms of oxygen ionic conductivity should be found within the group of $A^{3+}B^{3+}O_3$ perovskites and should be of cubic structure. This in turn seems to be impossible, because of the afore-mentioned observations made by Roth [33] and Muller and Roy [29], that the ideal cubic structure does not occur for the $A^{3+}B^{3+}O_3$ perovskites at room temperature. However, at elevated temperatures perovskites tend to transform their crystal structure to higher symmetries.

The BO_6 octahedra build up a three-dimensional network throughout the perovskite structure ABO_3 and electronic conduction proceeds via electrons or holes along the B–O–B chains. Because of polarization of the anion a covalent bond is formed between the oxygen ions and B-site cations. Therefore, the electrical properties of perovskites are supposed to be closely related to the covalency of the B–O–B bond. The degree of polarization depends on the polarizing power of the cation. Goldschmidt [36] suggested measuring the polarizing power by the Coulomb-potential Ze^2/r, where Z is the formal valence, e the elementary charge, and r the radius. For similar valence states a larger ionic radius decreases the Coulomb-potential. Figure 6 shows schematically the orbitals of an oxygen ion and an adjacent B-site cation which are thought to be responsible for the electron/hole exchange. The anionic p_σ orbitals are strongly attracted by the nuclear charge of the cation and combine tightly with the p_σ orbitals of the

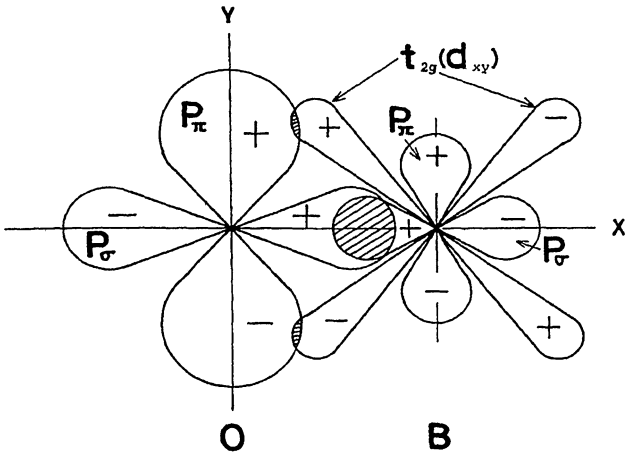

Fig. 6 Covalent bonds between the oxygen ion p_π-orbitals and B-cation t_{2g} (d) orbitals [66]

cation. This colinear overlap is the major part of the overall B–O bonding and strongly screens the t_{2g} orbitals of the B cation. Thus the t_{2g} orbitals spread towards the p_π orbitals of the oxygen ion and both orbitals might overlap. If so, the d-electrons of the t_{2g} orbital are permitted to drift into the t_{2g} orbital of a neighboring B-cation through the p_π orbital of the intermediate oxygen ion. This condition represents the state of itinerant electrons [66] which leads to electron/hole transport.

An early approach used to classify the conduction behavior of perovskites was that of Kamata et al. [66]. In this work, a diagram for simple ABO_3 perovskites is plotted with the ordinate Z_B/r_B and the abscissa Z_A/r_A, where Z_A (or Z_B) is the formal valence and r_A (or r_B) is the radius of the A ion (or B ion). This potential map of perovskites is shown in Fig. 7 for simple perovskites including information about their electrical conductance. By adding the states of the d-electrons at room temperature (localized: semi-conducting character; itinerant: metallic character) to each perovskite material a line can be drawn between the two distinct areas of different conduction behavior. It is obvious that the smaller the values of Z_A/r_A and Z_B/r_B the more itinerant the d-electrons of the perovskite become. A decreased B-site Coulomb potential causes a further spreading of the orbitals and, therefore, also a larger overlap integral leading to a more itinerant state. However, the A-site ion also attracts the anionic orbitals. An increasing A-site Coulomb-potential reduces the overlap integral between the anionic p_π and the B-site cationic t_{2g} orbitals leading to more localized state of the d-electrons.

Considering the potential map of perovskites (Fig. 7) and the previously mentioned tunability of the properties of perovskites, conclusions can be drawn how to influence the conduction behavior. By partly substituting ions on the A site and/or on the B site of the perovskite the conduction

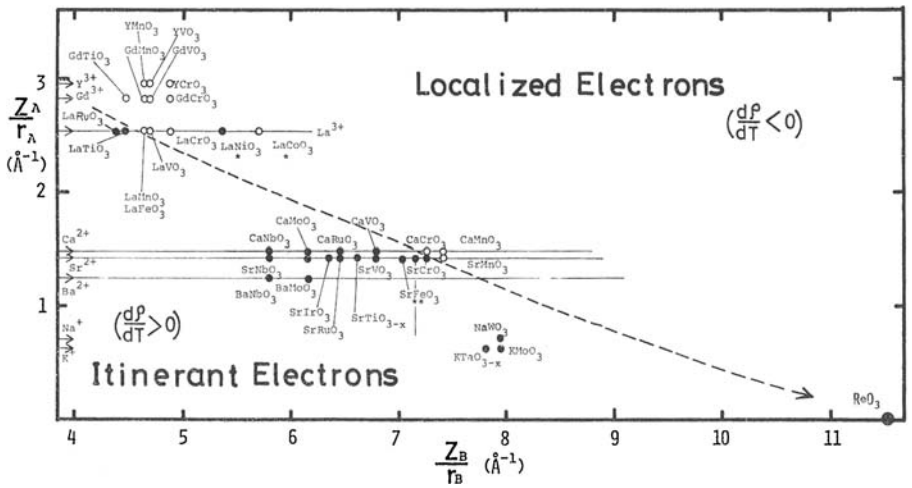

Fig. 7 Potential map of perovskites after Kamata et al. [66]

behavior can possibly be influenced because of a change of the integral overlap of the orbitals. A-site substitution with an ion having the same valence shifts the position in the potential map, only depending on the radius of the A ion, vertically. B-site substitution with an ion having the same valence, but different radius, shifts the position of the perovskite horizontally. A more complex situation arises from substitution on the A-site with an ion of different valence (and radius). To maintain electrical neutrality, the valence change introduced by the A-site has to be compensated either by a multivalent B-site cation (transition metal) or by creating vacancies on the oxygen sublattice. Because the oxygen deficiency/excess is not known for the single compositions here we only consider the valence change of the B site as the material's reaction. The radius of the transition metal also depends on its valence state. Therefore, aliovalent A-site substitution will result in a diagonal position change of the materials position in the potential map.

Using the approach of Kamata et al. [66] and Shannon's set of ionic radii [42] a structural field map can easily be created [1, 67] containing any simple perovskite material $ABO_{3-\delta}$. To include more complicated perovskites $A'_{1-x}A''_xB'_{1-y}B''_yO_{3-\delta}$, i.e. perovskites with partly substituted A and/or B sites, the nominal valences and radii have to be calculated as a weighted average. The resulting potential Z/r is calculated as average valence divided by average radius. This has been done for specific perovskite compositions using the data in Table 1 to derive a potential map (Fig. 8) which includes more complex perovskites.

The described diagonal position change of the perovskite because of aliovalent A-site substitution (La^{3+} is substituted by Sr^{2+}) can be observed for LSC, LSF, LSM, and LSCF in Fig. 8. End members with $x = 0$, i.e. $LaCoO_{3-\delta}$, $LaFeO_{3-\delta}$, $LaMnO_{3-\delta}$, and $LaCo_{0.5}Fe_{0.5}O_{3-\delta}$ are located on the top left in the potential map. If stoichiometry

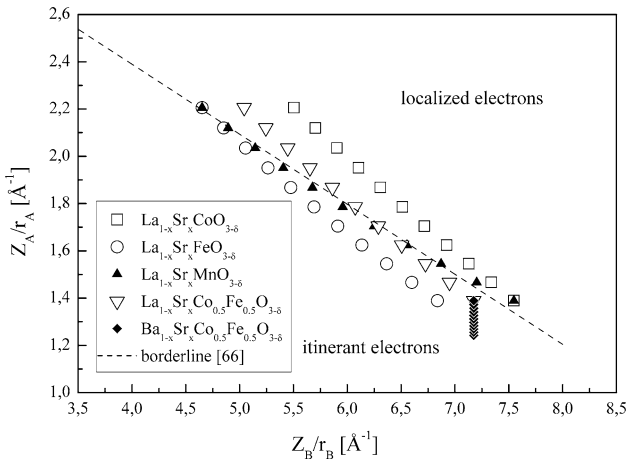

Fig. 8 Potential map of perovskites including more complex compositions

is assumed ($\delta = 0$) the transition metals at the B site have a threefold valence state. On increasing x in $La_{1-x}Sr_xBO_{3-\delta}$ the transition metal changes to a mixed valence state $3 + x$. Compared with the threefold valence state the radii of the transition metals are reduced in the fourfold valence state. Eventually Z_B/r_B is larger for higher valence states, which shifts the position to the right. Simultaneously the opposite process happens at the A site. Reducing valence state and increasing radius from La^{3+} to Sr^{2+} results in lower values of Z_A/r_A, i.e. in a position shift downwards. Finally, the position of the perovskite in the potential map moves diagonally from the top left to the lower right. Because the Sr and Ba ions are both divalent in BSCF, there is only a vertical shift in the position depending on the radius-change between Sr^{2+} and Ba^{2+}.

It is an interesting observation that good SOFC cathode materials are located relatively close to the borderline between metallic and semi-conducting perovskites, as

already reported [1]. This raises the question, of whether there is a physical reason, i.e. the electronic state of the three-dimensional-electrons, which plays an important role during the reduction of oxygen molecules to oxygen ions.

The model series LSM is located very close to the borderline of the different temperature dependences of the conductivity. As reported in the literature, $La_{1-x}Sr_xMnO_{3-\delta}$ has semi-conducting behavior for $0 \leq x \leq 0.5$ from room temperature up to 950 °C, which can be attributed to the small polaron hopping model [68] and $(La_{1-x}Sr_x)_{0.85}MnO_{3-\delta}$ changes its conduction mechanism (i.e. crossing the borderline) from semi-conducting to metallic behavior for $x = 0.5$ [69]. At elevated temperatures (above 1,000 °C) the conductivity of LSM becomes nearly constant with temperature and the conductivity shows a transition from positive to negative temperature dependence when the LSM contains 20 mol% Sr^{2+} [52]. Although the $La_{1-x}Sr_xCoO_{3-\delta}$ perovskites are located in the semi-conducting area of the potential map, Petric et al. [18] demonstrated that they show metallic conduction behavior for $0.2 \leq x \leq 0.9$ in the temperature range from 300 to 1,000 °C. The transition from semi-conducting to metallic behavior occurs at lower temperatures for increasing x. Another investigation confirms the change from semi-conducting to metallic character at $x = 0.25$. This goes along with abrupt crystal structure changes [20], which also affect the orbital overlap. No change in lattice symmetry was observable but the Co–O distance abruptly decreased and the Co–O–Co bond angle abruptly increased. The end member $LaCoO_{3-\delta}$ has semi-conducting behavior which changes to metallic behavior at elevated temperatures [70]. $LaFeO_{3-\delta}$ is located almost on the borderline of the potential map. An increasing level of substitution of La^{3+} by Sr^{2+} suggests the materials become more itinerant. For $La_{0.8}Sr_{0.2}FeO_{3-\delta}$ the conductivity increases with increasing temperature but decreases again at temperatures above 700 °C. At higher levels of Sr substitution the conductivity shows a negative temperature coefficient in the temperature range from 500 °C to 1,000 °C [17]. $La_{0.6}Sr_{0.4}Co_{0.2}Fe_{0.8}O_{3-\delta}$ has semi-conducting behavior up to approximately 600 °C and a decrease in conductivity with increasing temperature at temperatures higher than 600 °C [21].

Considering the aforementioned results, it should be discussed whether the potential map of perovskites is also applicable for more complex perovskite materials. As long as the ions at the A site (A′ and A″) and B site (B′ and B″) are randomly distributed within the substituted perovskite $A'_{1-x}A''_xB'_{1-y}B''_yO_{3-\delta}$, the approach used to calculate the weighted average of valences and radii seems to be justified. However, when B-site ordering occurs (which is likely for, e.g., $AB'_{0.5}B''_{0.5}O_{3-\delta}$) the situation becomes somewhat different. Figure 9 depicts schematically the B–O–B chains for $ABO_{3-\delta}$ (lattice parameter a_0) and $AB'_{0.5}B''_{0.5}O_{3-\delta}$ (lattice

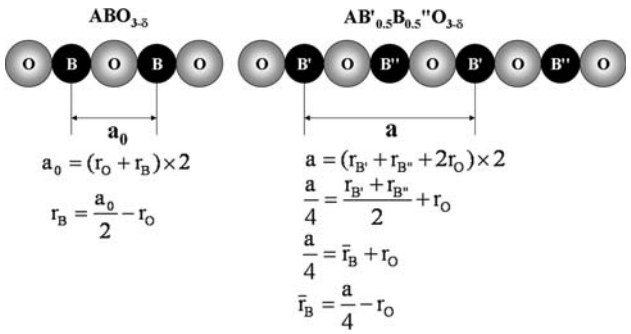

Fig. 9 B-site cation radius calculation for simple and B-site ordered perovskites

parameter a). Because the periodic length of the collinear chains is almost doubled for B-site-ordered perovskites, the relationship of the lattice parameters becomes $a \approx 2a_0$. B-site cation ordering is accompanied by energy stabilization and lattice contraction ($a \leq 2a_0$) is very likely.

Another important factor affecting the spreading and overlapping of the orbitals is the degree of distortion from the ideal cubic structure. It has been already described that the bond angle of the linear B–O–B-bond (180°) in a perfect cubic structure decreases when drifting away from ideal cubic symmetry. With a decrease of the average radius of the A site ion the BO_6 octahedra start to tilt and rotate to reduce the excess space around the A-site [71] resulting in B–O–B bond angles less than 180°. This movement narrows the conduction band and increases the band gap [72], i.e. it results in semi-conducting behavior. For LSC an expansion of the Co–O–Co bond angle towards 180° goes along with a broadening of the electronic bandwidths. This induces the transition from semi-conducting (insulating) to metallic character caused by the closing of the charge-transfer gap [73]. For LSM incorporation of Sr^{2+} enlarges the average A-site radius and also increases the amount of Mn^{4+} ions acting as charge carriers. The smaller radius of Mn^{4+} relative to Mn^{3+} reduces the Mn–Mn distance and results in the Mn–O–Mn bond angle approaching 180° [68].

Furthermore, knowledge of the valence states of the constituent ions is essential, because it also affects the final position of the compounds. However, if multivalent ions are included (e.g. transition metals at the B-site of the perovskite) it is difficult to obtain the correct valence state. Even when the valence state of the A-site cation is fixed (e.g. La^{3+}, Sr^{2+}), the valence state of the B-site cation is not certainly fixed in order to keep the charge balance of the perovskite. Grundy et al. [74] reported and modeled a disproportionation of Mn^{3+} into Mn^{2+} and Mn^{4+} for LSM. Oxygen-nonstoichiometry also plays an important role, because the charge imbalance caused by an aliovalent substitution of the A-site ion will either be balanced by a valence change of the transition metal or by the

formation of vacancies, or both, to an unknown extent. In $Ba_{1-x}Sr_xCo_{1-y}Fe_yO_{3-\delta}$ the valance state ratio 3+/4+ of the transition metal ions as a function of temperature was analyzed by X-ray adsorption spectroscopy and Mössbauer spectroscopy and revealed a 3+ majority up to 800 °C [75]. X-ray adsorption spectroscopy was also used to analyze the spin states of Fe and Co in BSCF, which were in high spin and intermediate spin, respectively, at round 800 °C [76]. The technique has also be used to analyze the electronic properties of Co and Fe in $La_{0.5}Sr_{0.5}Fe_{1-x}M_xO_{3-\delta}$ with M = Ti or Ta and $x = 0$, 0.1, and 0.2 [77]. The spin state of Fe and Co determines the effective ionic radii of the ion and thus is an important property. The two aforementioned criteria, i.e. the true radii and valence state, are essential for the correct position of the perovskites within the potential field map. Inaccurate values or uncertainties will certainly cause deviations and will eventually lead to a wrong position or an area of probability rather than a single point. In order to correctly apply the approach of the potential map to any perovskite material, it is necessary to know the previously mentioned information about the candidate material, for example valence states and ionic radii. Also the validity of the map and the proposed transition line for elevated temperatures (e.g. 500 °C to 1,000 °C) is not yet proven.

Miscellaneous perovskite materials show a decreasing conductivity at elevated temperatures. This decrease in conductivity is often interpreted as a semi-conductor–metal transition. Increasing temperatures cause changes in the crystal structure towards higher symmetries and the transition temperature is affected by the composition [48]. However, because of those structural changes the integral orbital overlap might be affected and cause a sudden change in the temperature-dependence of the conductivity. For $La_{1-x}Sr_xCoO_{3-\delta}$ the transition from semi-conducting to metallic behavior has been attributed to the abrupt changes in the crystal structure (Co–O bond lengths and Co–O–Co bond angles) and the corresponding increase of the integral orbital overlap [20]. Another explanation suggests that a change in the amount of charge carriers causes different temperature dependence of the conductivity. Because of elevated temperatures an oxygen vacancy formation occurs which is accompanied by a reduced number of holes acting as the charge carriers [21, 50, 78]. For each oxygen ion leaving the lattice two electron holes are eliminated and Eq. 5 has to be modified to account for a variable amount of charge carriers:

$$\sigma = \left\{[(A' - 2\delta)C']/T^{S}\right\}\exp(-E_a/kT) \quad (8)$$

The temperature-dependent carrier concentration is now included in the new term in the pre-exponential factor. Thereby, the initial concentration of charge carriers (A') which has been created by acceptor doping on the A site is reduced by 2δ, where δ is the temperature-dependent oxygen vacancy concentration [50]. Although the state of the charge carriers does not change, their decreasing amount results in reduced conductivity. This could be misinterpreted as a transition from the semi-conducting to the itinerant state.

An approach similar to the potential field map was proposed by Fujimori [79] and later re-examined by Inoue [32]. They studied the electronic structure of three-dimensional transition metals with a metal–insulator transition as a function of the chemical composition. Starting from an insulating transition metal oxide (where the three-dimensional electrons are localized) metallic conductivity can be achieved in two ways. On the one hand a band-gap closure can occur by diminishing the splitting between the band-gaps or increasing the band widths. On the other hand a valence change of the transition metal ions can be initiated to introduce extra electron or hole carriers into the insulating host system [79]. The band gap of the host insulator can either be *d–d* Mott–Hubbard type or ligand–p to metal–*d* charge-transfer type. This depends on the magnitudes of the *d–d* Coulomb repulsion energy U and the p-to-d charge-transfer energy Δ. This approach is more sophisticated than the potential map of perovskites. However, it also deals with metal–insulator transitions as functions of chemical composition.

Oxygen diffusion coefficient D and surface exchange coefficient k

It is generally assumed today, but not fully proven, that SOFC cathode materials should favorably be mixed ionic electronic conductors (MIEC), i.e. electron and oxygen ion conductors in parallel. If the SOFC cathode material is a pure electronic conductor the oxygen reduction reaction is limited to the three-phase boundary (TPB) where cathode, electrolyte, and the oxygen-containing atmosphere meet. There is only one possible mechanism for the oxygen reduction: the oxygen is adsorbed at the surface of the cathode and diffuses via surface diffusion towards the TPB where it becomes charged and incorporated into the electrolyte [1]. If the cathode material of the SOFC is a MIEC, the kinetics of the oxygen reduction are supposed to be enhanced, because the material provides the active site for reduction at the surface and also a pathway for oxygen ion diffusion through the bulk. In this case there are two parallel pathways for incorporation of the oxygen into the solid material: the surface pathway to the TPB and the bulk pathway (Fig. 10). Following the surface pathway the oxygen molecule will be adsorbed at the surface of the MIEC and transported via surface diffusion towards the TPB (black dot in Fig. 10) where the transfer step into

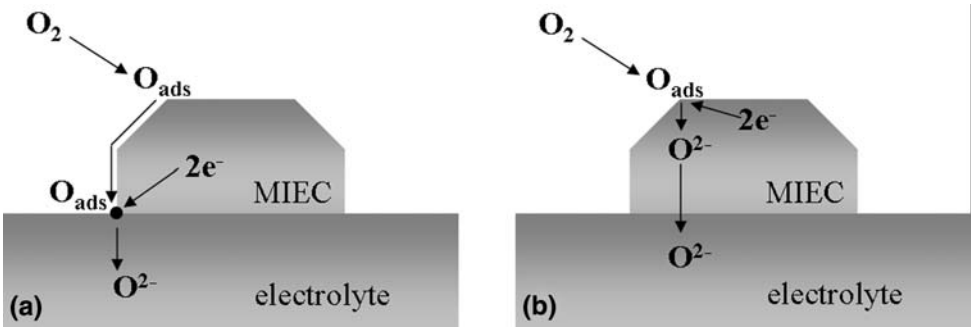

Fig. 10 Surface pathway **a** versus bulk pathway **b**

the electrolyte occurs. If substantial ionic conductivity exists in the MIEC the transport via the bulk pathway can also occur. After adsorption of the oxygen molecule the charge-transfer step occurs at the cathode surface so that the adsorbed atoms turn into oxygen ions which will be directly incorporated into the cathode material.

Transport within the cathode occurs via oxygen ionic conductivity until the ions are transferred into the electrolyte material. This is synonymous with an increase of the TPB, because the whole cathode surface may be available for the charge-transfer step. However, so far there is no final agreement with regard to the rate-determining step [12].

If the oxygen ionic conductivity is relatively low (as in the case of LSM), the MIEC behaves similar to a pure electronic conductor [1], i.e. oxygen transport will occur via the surface pathway to the TPB. Good ionic conductivity, on the other hand, leads to transport of oxygen via the bulk pathway. This is supposed to increase the reaction zone and reduce the polarization resistance [12, 80, 81]. However, the two important material properties which describe the aforementioned steps, namely the incorporation of oxygen ions into the material and the transport of oxygen ions within the material, are the oxygen surface exchange coefficient k (cm s^{-1}) and the oxygen diffusion coefficient D (cm^2 s^{-1}), respectively. It is known that both have different activation energies, i.e. within certain temperature ranges one of them is determining the performance of the material. Ullmann et al. [82] reported for membranes that surface exchange often has higher activation energies than oxygen diffusion. Oxygen exchange is, therefore, likely to be rate limiting in lower temperature regions whereas the diffusion process limits the performance at elevated temperatures [82]. On the other hand, Kilner et al. [83] found the activation enthalpy of the surface exchange coefficient to be lower than that for the self-diffusion coefficient. This contradiction shows that the processes are not yet well understood. Kilner et al. [83] also reported a strong correlation between k and D. This leads to the suggestion that good oxygen ion conductors also have good oxygen-exchange properties. Another investigation on perovskites revealed a dependence of k on the oxygen nonstoichiometry [84]. This implies that both surface exchange and diffusion are dependent on the presence of vacancies in the oxygen sublattice. However, in order to obtain well performing cathode materials the compositions should have high oxygen-exchange capacities for an easy incorporation of oxygen ions into their lattices and high oxygen diffusivity in order to ensure fast transport of the oxygen ions through their lattice.

Diffusion and surface exchange coefficients can be determined by several different methods [85]. Isotope exchange techniques (which apply secondary ion mass spectrometry to trace the isotopically labeled $^{18}O_2$ exchange gas) measure the oxygen self-diffusion or tracer diffusion coefficients, D or D^*, respectively, and the surface exchange coefficients k or k^*, respectively [83, 86–90]. There are also electrochemical polarization or relaxation methods. The conductivity relaxation method uses the fact that a change in the oxygen partial pressure results in a change in electronic conductivity [91–94]. Using appropriate diffusion models the chemical diffusion coefficient and surface exchange coefficient $\tilde{D}$ and $\tilde{k}$, can be obtained [85]. Also electrochemical impedance spectroscopy can be applied [80, 81, 95].

A collection of $\tilde{k}$ and $\tilde{D}$-values as derived by tracer diffusion or conductivity relaxation is given in Table 2. The data are sometimes contradictory, and no tendencies have yet been observed which might describe a dependence of k or D on composition. Even for the same material (e.g. $La_{0.6}Sr_{0.4}Co_{0.2}Fe_{0.8}O_{3-\delta}$) the values for the surface exchange coefficient vary by orders of magnitude. This shows that not only are the mechanisms and kinetics of the oxygen reduction still under question, but also that the procedures used to measure k and D can be improved, because the results obtained by the different measurement techniques are not conclusive.

Another strategy for approaching the problem of fast surface exchange deals with the work function. The work function is the minimum energy required to remove an electron from the solid (Fermi energy level) to the vacuum (reference level or zero level) [96], i.e. to release

Table 2 Literature data for chemical diffusion coefficient $\widetilde{D}$ and surface exchange coefficient $\tilde{k}$, as derived by tracer diffusion [92, 93] or conductivity relaxation [91, 100–106]

Composition	$\tilde{k}$/cm s^{-1}	$\tilde{D}$/cm^2 s^{-1}	T/K	$p(O_2)$/bar	Ref.
$La_{0.8}Sr_{0.2}MnO_{3-\delta}$	–	5.0×10^{-07}	1,073	–	[100]
$La_{0.5}Sr_{0.5}FeO_{3-\delta}$	4.0×10^{-04}	6.4×10^{-06}	1,061	0.20	[101]
$La_{0.6}Sr_{0.4}FeO_{3-\delta}$	–	1.0×10^{-05}	1,073	–	[102]
$La_{0.6}Sr_{0.4}FeO_{3-\delta}$	1.0×10^{-03}	1.1×10^{-05}	1,073	0.21	[91]
$La_{0.6}Sr_{0.4}CoO_{3-\delta}$	2.5×10^{-04}	2.5×10^{-06}	1,098	0.002	[103]
$La_{0.6}Sr_{0.4}Co_{0.5}Fe_{0.5}O_{3-\delta}$	1.8×10^{-03}	5.6×10^{-06}	1,073	0.21	[104]
$La_{0.6}Sr_{0.4}Co_{0.2}Fe_{0.8}O_{3-\delta}$	–	7.8×10^{-06}	1,073	–	[105]
$La_{0.6}Sr_{0.4}Co_{0.2}Fe_{0.8}O_{3-\delta}$	1.5×10^{-03}	8.3×10^{-06}	1,073	0.21	[106]
$La_{0.6}Sr_{0.4}Co_{0.2}Fe_{0.8}O_{3-\delta}$	3.8×10^{-05}	1.1×10^{-05}	1,073	0.21	[92]
$La_{0.6}Sr_{0.4}Co_{0.2}Fe_{0.8}O_{3-\delta}$	1.6×10^{-04}	7.9×10^{-06}	1,073	0.21	[93]
$Ba_{0.5}Sr_{0.5}Co_{0.8}Fe_{0.2}O_{3-\delta}$	–	1.7×10^{-06}	1,073	–	[105]
$Ba_{0.5}Sr_{0.5}Co_{0.8}Fe_{0.2}O_{3-\delta}$	–	2.9×10^{-06}	1,073	–	[106]
$Pr_{0.6}Sr_{0.4}Co_{0.2}Fe_{0.8}O_{3-\delta}$	–	5.6×10^{-06}	1,073	–	[102]

electrons from the cathode surface in order to reduce the incoming oxygen molecules into ions and start the process of oxygen incorporation. The work function itself has a very complex physical meaning [97] and is affected by various surface effects. However, a lower work function, i.e. less energy needed to release the electron, is desirable for rapid initiation of the charge-transfer step and, therefore, oxygen reduction. Measurements of the work function may be used to monitor surface reactions [98] which occur at the cathode during the adsorption and dissociation of the oxygen. Chemisorption of oxygen generates an electrical surface barrier which leads to a decrease in the chemical potential of the electrons in the surface layer. This results in retardation of the process of further ionization which is necessary to obtain doubly charged oxygen ions which can be incorporated into the surface layer [99]. Therefore, it seems desirable to keep the generated surface barrier to a minimum in order to obtain high-performance cathodes. Obviously, the work function is correlated with the oxygen-exchange coefficient. Low work functions will supposedly result in large oxygen-exchange coefficients k.

Conclusions

The tunability of the perovskite structure allows the substitution of constituent ions over a wide range. Goldschmidt's tolerance factor is a guideline for predicting whether the desired composition forms a perovskite structure. Other calculations on the basis of ionic radii, for example the pseudo-cubic lattice parameter a_0, the critical radius r_{cr}, or the lattice free cell volume V_f, are used solely to estimate the evolution of a specific property. They are basically calculated from the ionic radii of the A and the B-site cations, r_A and r_B, respectively. There is, therefore, some redundancy between these properties and trends are sometimes inconclusive.

The basic principles of alteration of the partial ionic and electronic conductivities of perovskite oxides are reasonably understood. In order to enhance the ionic conductivity no multivalent B-site cations should be incorporated, so aliovalent A-site substitution preferably results in the formation of oxygen vacancies. Increasing the number of oxygen vacancies leads to an increase of the oxygen ionic conductivity. The electronic conductivity takes place along the B–O–B bonds, because of the valence change of the B-site transition metal cations. A large amount of charge carriers (e.g. a ratio TM^{3+}/TM^{4+} close to unity) enhances the electronic conductivity.

The application of the potential field map as a tool to predict the conduction behavior of perovskite materials was discussed, and tailoring the materials to be in transition state between metal and semiconductor seems to be advantageous. For substituted perovskites, especially, it is still challenging to find the correct position for a perovskite within the potential map, because the exact valence states of the constituent ions need to be known. For compositions $A'_{1-x}A''_xB'_{1-y}B''_yO_{3-\delta}$ calculation of the radius as a weighted average might not be justified. These challenges must be solved in order to investigate whether the potential map can be reliably used.

Furthermore, oxygen surface exchange and oxygen diffusion are important properties of these materials. Increasing these coefficients enhances the oxygen reduction process at the cathode. However, exact values are difficult to obtain. The application of mixed ionic electronic conductors is supposed to increase the reaction zone for the reduction of oxygen from the three-phase boundary to the cathode surface.

Acknowledgments The authors thank Professor Werner Sitte, Montanuniversität Leoben, and Peter Ried, Montanuniversität Leoben and Empa, Laboratory for High Performance Ceramics, for their input on the oxygen exchange and transport properties.

References

1. Gauckler LJ, Beckel D, Buergler BE, Jud E, Muecke UP, Prestat M, Rupp JLM, Richter J (2004) Chimia 58:837–850
2. Minh NQ (1993) J Am Ceram Soc 76:563–588
3. Steele BCH (2000) Solid State Ionics 134:3–20
4. Steele BCH (1994) J Power Source 49:1–14
5. Singhal SC, Kendall K (eds) (2003) High temperature solid oxide fuel cells: fundamentals, design and applications, p 405, Elsevier
6. Singhal SC (2000) Solid State Ionics 135:305–313
7. Bucher E, Egger A, Caraman GB, Sitte W (2008) J Electrochem Soc 155:B1218–B1224
8. Baumann FS (2006) Ph.D. thesis, Fakultät für Chemie, Universität Stuttgart
9. Simner SP, Bonnett JF, Canfield NL, Meinhardt KD, Shelton JP, Sprenkle VL, Stevenson JW (2003) J Power Sources 113:1–10
10. Petitjean M, Caboche G, Siebert E, Dessemond L, Dufour L-C (2005) J Eur Ceram Soc 25:2651–2654
11. Virkar AV, Chen J, Tanner CW, Kim J-W (2000) Solid State Ionics 131:189–198
12. Fleig J (2002) J Power Sources 105:228–238
13. Jiang SP (2002) Solid State Ionics 146:1–22
14. Haile SM (2003) Acta Mater 51:5981–6000
15. Mai A, Haanappel VAC, Uhlenbruck S, Tietz F, Stöver D (2005) Solid State Ionics 176:1341–1350
16. Simner SP, Bonnett JF, Canfield NL, Meinhardt KD, Sprenkle VL, Stevenson JW (2002) Electrochem Solid-State Lett 5:A173–A175
17. Bongio EV, Black H, Raszewski FC, Edwards D, McConville CJ, Amarakoon VRW (2005) J Electroceram 14:193–198
18. Petric A, Huang P, Tietz F (2000) Solid State Ionics 135:719–725
19. Holc J, Kuščer D, Hrovat M, Bernik S, Kolar D (1997) Solid State Ionics 95:259–268
20. Mineshige A, Inaba M, Yao T, Ogumi Z, Kikuchi K, Kawase M (1996) J Solid State Chem 121:423–429
21. Kostogloudis GC, Ftikos C (1999) Solid State Ionics 126:143–151
22. Teraoka Y, Nobunaga T, Okamoto K, Miura N, Yamazoe N (1991) Solid State Ionics 48:207–212
23. Shao Z, Haile SM (2004) Nature 431:170–173
24. Pena-Martinez J, Marrero-Lopez D, Ruiz-Morales JC, Buergler BE, Nunez P, Gauckler LJ (2006) J Power Sources 159:914–921
25. Li S, Lu Z, Wei B, Huang X, Miao J, Liu Z, Su W (2008) J Alloy Compd 448:116–121
26. Kostogloudis GC, Vasilakos N, Ftikos C (1997) J Eur Ceram Soc 17:1513–1521
27. Mogensen M, Jensen KV, Jørgensen MJ, Primdahl S (2002) Solid State Ionics 150:123–129
28. Patrakeev MV, Bahteeva JA, Mitberg EB, Leonidov IA, Kozhevnikov VL, Poeppelmeier KR (2003) J Solid State Chem 172:219–231
29. Muller O, Roy R (1974) The major ternary structural families. Springer, Heidelberg
30. Vyshatko NP, Kharton V, Shaula AL, Naumovich EN, Marques FMB (2003) Mater Res Bull 38:185–193
31. Mogensen M, Lybye D, Bonanos N, Hendriksen PV, Poulsen FW (2004) Solid State Ionics 174:279–286
32. Inoue IH (2005) Semicond Sci Technol 20:S112–S120
33. Roth RS (1957) J Res Natl Bur Stand 58:75–88
34. Li C, Soh KCK, Wu P (2004) J Alloy Compd 372:40–48
35. Attfield JP (2002) Engineering 5:427–438
36. Goldschmidt VM, Barth T, Lunde G, Zachariasen WH, VII: Die Gesetze der Krystallochemie. In: Geochemische Verteilungsgesetze der Elemente (Oslo, 1926)
37. Zachariasen WH (1931) Z Kristallogr 80:137–153
38. Pauling L (1927) J Am Chem Soc 49:765–790
39. Ahrens LH (1952) Geochim Cosmochim Acta 2:155–169
40. Shannon RD, Prewitt CT (1969) Acta Crystallogr Sect B B25:925–946
41. Shannon RD, Prewitt CT (1970) J Inorg Nucl Chem 32:1427–1441
42. Shannon RD (1976) Acta Crystallogr Sect A A 32:751–767
43. Hayashi H, Inaba H, Matsuyama M, Lan NG, Dokiya M, Tagawa H (1999) Solid State Ionics 122:1–15
44. Trofimenko N, Ullmann H (1999) Solid State Ionics 118:215–227
45. Xu S, Moritomo Y, Ohoyama K, Nakamura A (2003) J Phys Soc Jpn 72:709–712
46. Sundaresan A, Paulose PL, Mallik R, Sampathkumaran EV (1998) Phys Rev B 57:2690
47. Negas T, Roth RS (1970) J Solid State Chem 1:409–418
48. Fossdal A, Menon M, Waernhus I, Wiik K, Einarsrud M-A, Grande T (2004) J Am Ceram Soc 87:1952–1958
49. Attfield JP (2001) Int J Inorg Mater 3:1147–1152
50. Stevenson JW, Armstrong TR, Carneim RD, Pederson LR, Weber WJ (1996) J Electrochem Soc 143:2722–2729
51. Boivin JC, Mairesse G (1998) Chem Mater 10:2870–2888
52. Kuo JH, Anderson HU, Sparlin DM (1990) J Solid State Chem 87:55–63
53. van Roosmalen JAM, Cordfunke EHP (1994) J Solid State Chem 110:109–112
54. Huang X, Pei L, Liu Z, Lu Z, Sui Y, Qian Z, Su W (2002) J Alloy Compd 345:265–270
55. Gao W, Sammes NM (1999) An introduction to electronic and ionic materials. World Scientific Publishing, Singapore
56. He H, Huang X, Chen L (2001) Electrochim Acta 46:2871–2877
57. Ranløv J (1995) Ph.D. thesis, Materials Department, Technical University of Denmark
58. Cherry M, Islam MS, Catlow CRA (1995) J Solid State Chem 118:125–132
59. Kilner JA, Brook RJ (1982) Solid State Ionics 6:237–252
60. Fukunaga O, Fujita T (1973) J Solid State Chem 8:331–338
61. Islam MS, Cherry M, Catlow CRA (1996) J Solid State Chem 124:230–237
62. Sammells AF, Cook RL, White JH, Osborne JJ, MacDuff RC (1992) Solid State Ionics 52:111–123
63. Cook RL, Sammells AF (1991) Solid State Ionics 45:311–321
64. Lybye D, Poulsen FW, Mogensen M (2000) Solid State Ionics 128:91–103
65. Ranlov J, Bonanos N, Poulsen FW, Mogensen M (1994) Solid State Phenomena 39–40
66. Kamata K, Nakamura T, Sata T (1974) Bull Tokyo Instit Technol 120:73–79
67. Richter J, Holtappels P, Vogt U, Graule T, Gauckler LJ (2006) Solid State Ionics 177:3105–3108
68. van Roosmalen JAM, Huijsmans JPP, Plomp L (1993) Solid State Ionics 66:279–284
69. Hammouche A, Schouler EJL, Henault M (1988) Solid State Ionics 28–30:1205–1207
70. Kharton VV, Figueiredo FM, Kovalevski AV, Viskup AP, Naumovich EN, Yaremchenko AA, Bashmakov IA, Marques FMB (2001) J Eur Ceram Soc 21:2301–2309
71. Cherif K, Dhahri J, Dhahri E, Oumezzine M, Vincent H (2002) J Solid State Chem 163:466–471

72. Eng HW, Barnes PW, Auer BM, Woodward PM (2003) J Solid State Chem 175:94–109
73. Mineshige A, Kobune M, Fujii S, Ogumi Z, Inaba M, Yao T, Kikuchi K (1999) J Solid State Chem 142:374–381
74. Grundy AN, Hallstedt B, Gauckler LJ (2004) Calphad 28 computer coupling of phase diagrams and thermochemistry 28:191–201
75. Harvey AS, Litterst FJ, Yang Z, Rupp JLM, Infortuna A, Gauckler LJ (2009) Phys Chem Chem Phys 11:1–9
76. Harvey AS, Yang Z, Infortuna A, Beckel D, Purton JA, Gauckler LJ (2009) J Phys Condens Matter 21 (in press). doi: 10.1088/0953-8984/21/1/015801
77. Braun A, Bayraktar D, Harvey AS, Beckel D, Purton JA, Holtappels P, Gauckler LJ, Graule T (2009) Appl Phys Lett (accepted)
78. Kostogloudis GC, Ftikos C (2000) Solid State Ionics 135:537–541
79. Fujimori A (1992) J Phys Chem Solids 53:1595–1602
80. Prestat M, Koenig J-F, Gauckler L (2007) J Electroceram 18:87–101
81. Prestat M, Koenig JF, Gauckler JL (2007) J Electroceram 18:111–120
82. Ullmann H, Guth U, Vashook VV, Burckhardt W, Götz R, Bülow M (2005) Keramische Zeitschrift 2:72–78
83. Kilner JA, de Souza RA, Fullarton IC (1996) Solid State Ionics 86–88:703–709
84. Yasuda I, Hikita T (1994) J Electrochem Soc 141:1268–1273
85. Bucher E (2003) Dissertation Montanuniversität Leoben
86. Carter S, Selcuk A, Chater RJ, Kajda J, Kilner JA, Steele BCH (1992) Solid State Ionics 53–56:597–605
87. van Doorn RHE, Fullarton IC, de Souza RA, Kilner JA, Bouwmeester HJM, Burggraf AJ (1997) Solid State Ionics 96:1–7
88. de Souza RA, Kilner JA (1998) Solid State Ionics 106:175–187
89. de Souza RA, Kilner JA (1999) Solid State Ionics 126:153–161
90. Steele BCH (1995) Solid State Ionics 75:157–165
91. ten Elshof JE, Lankhorst MHR, Bouwmeester HJM (1997) J Electrochem Soc 144:1060–1067
92. Lane JA, Benson SJ, Waller D, Kilner JA (1999) Solid State Ionics 121:201–208
93. Lane JA, Kilner JA (2000) Solid State Ionics 136–137:997–1001
94. Wang S, van der Heide PAW, Chavez C, Jacobson AJ, Adler SB (2003) Solid State Ionics 156:201–208
95. Adler SB (1998) Solid State Ionics 111:125–134
96. Cox PA (1987) The electronic structure and chemistry of solids. Oxford University Press, Oxford
97. Bak T, Nowotny J, Rekas M, Sorrell CC, Vance ER (2000) Solid State Ionics 135:563–565
98. Badwal SPS, Bak T, Jiang SP, Love J, Nowotny J, Rekas M, Sorrell CC, Vance ER (2001) J Phys Chem Solids 62:723–729
99. Bak T, Nowotny J, Rekas M, Sorrell CC (2001) J Phys Chem Solids 62:737–742
100. Bak T, Nowotny J, Rekas M, Sorrell CC, Vance ER (2000) Solid State Ionics 135:557–561
101. Yoo J, Verma A, Wang S, Jacobson AJ (2005) J Electrochem Soc 152:A497–A505
102. Vashook VV, Al Daroukh M, Ullmann H (2001) Ionics 7:59–66
103. Preis W, Bucher E, Sitte W (2002) J Power Sources 106:116–121
104. Bouwmeester HJM, Den Otter MW, Boukamp BA (2004) J Solid State Electrochem 8:599–605
105. Wang H, Cong Y, Yang W (2002) J Membr Sci 210:259–271
106. Lu H, Cong Y, Yang WS (2006) Solid State Ionics 177:595–600